The atomic-level structural differences between in-situ and ex-situ Fe(III) co-precipitates determine their coagulation behaviour in phosphate and DOM removal

Bingqian Yang [a,b], Nigel Graham [c], Peng Liu [d], Mengjie Liu [a,b], John Gregory [e], and Wenzheng Yu [a*]

[a] State Key Laboratory of Environmental Aquatic Chemistry, Key Laboratory of Drinking Water Science and Technology, Research Center for Eco-Environmental Sciences, Chinese Academy of Sciences, Beijing 100085, People's Republic of China (wzyu@rcees.ac.cn)

[b] College of Resources and Environment, University of Chinese Academy of Sciences (UCAS), Beijing 100049, China

[c] Department of Civil and Environmental Engineering, Imperial College London, South Kensington Campus, London SW7 2AZ, United Kingdom (n.graham@imperial.ac.uk)

[d] School of Environmental Studies, China University of Geosciences, Wuhan, 430074, China

[e] Department of Civil, Environmental & Geomatic Engineering, University College London

Abstract

The in-situ Fe(III) co-precipitation from Fe^{2+} oxidation is a widespread phenomenon in both natural environments and water treatment processes. Studies have shown the superiority of in-situ Fe(III) over ex-situ Fe(III) in coagulation, but its reason remains unclear due to the uncertain nature of amorphous structures. Here, we utilized an in-situ Fe(III) coagulation process that oxidated Fe(II) coagulant through potassium permanganate ($KMnO_4$) to treat phosphate-containing surface water and analyzed differences between in-situ and ex-situ Fe(III) coagulants in phosphate removal, dissolved organic matter (DOM) removal, and floc growth. Compared to ex-situ Fe(III) generated by Fe^{3+} coagulant, flocs formed by natural oxidating Fe^{2+} coagulant exhibited more effective phosphate removal. Furthermore, in-situ Fe(III) formed through accelerated oxidation of Fe^{2+} with $KMnO_4$ had an improved flocculation behavior and enhanced removal of specific types of DOM by forming a more stable structure while still maintaining effective phosphate removal. The Fe K-edge extended X-ray absorption fine structure spectra (EXAFS) of flocs explained their differences. A short-range ordered strengite-like structure (corner-linked PO_4 tetrahedra to FeO_6 octahedra) was the key to a more effective phosphorus removal of in-situ Fe(III) than ex-situ Fe(III), and was well preserved when $KMnO_4$ accelerated in-situ Fe(III) formation. Conversely, $KMnO_4$ significantly inhibited the edge and corner coordination between FeO_6 octahedra and altered the floc chain-forming behavior by accelerating hydrolysis, resulting in a more dispersed monomeric structure than ex-situ Fe(III). This research provides an explanation for the superiority of in-situ Fe(III) in phosphorus removal and highlights the importance of atomic-level structural differences between ex-situ and in-situ Fe(III) co-precipitates in water treatment.

Keywords: Lepidocrocite; coagulation; phosphate; in-situ Fe; Fe precipitation; EXAFS; wavelet transform

Synopsis:

The atomic-level structural changes of flocs reveal the advantages of in-situ Fe(III), formed in Fe(II)-$KMnO_4$ processes, for DOM and phosphorus removal.

1. Introduction

As an essential element in living organisms, phosphorus has a critical impact on the aqueous environment. Compared to other essential nutrients, phosphorus has a low relative abundance and is dubbed "life's bottleneck".[1] Since the Industrial Revolution, with the increase of the world's population, the balance of phosphorus has been seriously altered, and the existence of too much or too little phosphorus can cause problems.[2] On the one hand, phosphorus fertilizer resources are scarce and unevenly distributed; the shortage of phosphorus can cause a series of societal issues, such as food insecurity. On the other hand, soil erosion and the uncontrolled application of phosphate fertilizers can lead to excessive phosphorus content in surface water and municipal sewage, causing environmental and ecological problems, such as eutrophication.[3] Highly effective methods for phosphorus removal are urgently required.[4]

Iron salt coagulants are often used to treat phosphorus-containing organic-laden water as a well-established low-cost water treatment process.[5] At present, the widely used iron salt coagulants include Fe(II) and Fe(III).[6] Oxidation of Fe^{2+} is also a very effective coagulation arrangement, using oxidants such as hydrogen peroxide, persulfate, and potassium permanganate ($KMnO_4$).[7] Compared with adding Fe(III) coagulants directly to form ex-situ Fe(III), the Fe(III) formed by Fe^{2+} coagulant through in-situ oxidation is more effective under certain conditions, such as removing phosphate and arsenate.[8] However, the reasons for the greater performance of in-situ Fe(III) than ex-situ Fe(III) are still unclear.[9] Previous studies have mainly focused on the properties of crystals, while the influence of different degrees of oxidation on the structure of Fe-phosphate amorphous co-precipitation still requires further

investigation.[14] Conventional analytical methods cannot easily distinguish the differences between in-situ Fe(III) and ex-situ Fe(III) amorphous structures. When enhancing the removal of phosphate, the effect on the Fe structure must not be ignored. An in-depth study of the in-situ Fe(III) formation can advance our understanding of the intrinsic coagulation mechanism.

As a critical link in the Fe cycle, in-situ amorphous or low-crystallinity ferric precipitates formed by the oxidation of Fe^{2+} are very common in nature and have been extensively studied. Andreas et al. found that the presence of phosphate hinders the formation of crystalline products.[10] It was reported by Mikutta et al. that the microstructure of the amorphous iron phosphate was similar to strengite, in which FeO_6 hexahedrons formed corner coordination with PO_4.[11] Senn et al. identified the possible co-precipitate products during the Fe(II) oxidation process in a phosphate environment, including lepidocrocite, amorphous ferric phosphate, and phosphate-rich iron oxyhydroxide.[12, 13] Some studies have also investigated the effect of inorganic ions (e.g., Ca, Si, Mn, and As) on this process.[14, 15] Although these geoscientific findings may shed light on the coagulation mechanism involving Fe salts, the actual coagulation process is more complicated. For instance, oxidizing agents and organics play an essential role in forming amorphous Fe-phosphates from Fe^{2+}, which further influences its effect on nutrient retention and coagulation efficiency.[16] Therefore, the role of these substances needs further investigation.

In this study, we used an in-situ Fe(III) coagulation process that oxidated Fe(II) coagulant through $KMnO_4$ in situ to treat surface water that contained phosphates. We investigated the mechanism at the atomic level by scrutinizing the structural differences between in-situ and ex-situ Fe(III) precipitates. Here, ex-situ Fe(III) refers to the precipitated iron oxides, along

with co-precipitates and adsorbed species formed when a Fe(III) coagulant salt was dosed. In contrast, in-situ Fe(III) refers to the Fe(III) solids formed by oxidizing Fe(II) through variable $KMnO_4$ dosages when a Fe(II) coagulant salt is added to the process water. The differences in coagulation between Fe(II)-$KMnO_4$ and conventional Fe(III) and Fe(II) coagulants were compared based on three factors: floc formation, dissolved organic matter (DOM) removal, and phosphate behavior. Specifically, we measured floc agglomeration and growth behavior, quantified changes in the composition, concentration, and molecular weight of DOM, and analyzed the binding mode of phosphate to flocs. Additionally, the coagulation difference when treating surface water with and without phosphorus was also compared. Furthermore, we scrutinized the phosphate binding mode in co-precipitation formed through varying degrees of oxidation by employing 2D-COS FTIR. Lastly, to better understand the key role played by the coordination structure of Fe atoms in rapidly formed in-situ Fe(III) when removing phosphate and DOM, linear fitting, wavelet transform (WT), and shell fitting of EXAFS data were employed.

2. Methods

Coagulation Experiments

The test solution, containing 2 mg/L phosphorus, was obtained by adding $Na_2HPO_4{\cdot}2H_2O$ to the surface water sample. The dosing scheme of coagulants and the properties of the raw water are presented in Text S1 and Table 1. The direct addition of $Fe_2(SO_4)_3$ and $FeSO_4$ represented the control groups for ex-situ Fe(III) and in-situ Fe(III) without $KMnO_4$, respectively, with a fixed coagulant concentration of 0.2 mmol Fe/L. To adjust the molar ratio of Fe to Mn, we varied the dosage of $KMnO_4$ while keeping the concentration of Fe^{2+} fixed at 0.2 mmol Fe/L. For instance, we added 0.066 mmol/L of $KMnO_4$ when the Fe(II): Mn ratio was 1:0.33, which attained the stoichiometric ratio of the reaction (Eqs 1). These coagulants were employed to treat surface waters with and without phosphate, and their coagulation behavior was examined. The experimental steps and controlled conditions are outlined in Text S2 and Figure S1. After coagulation, the reacted solution and floc products were separated and collected for analysis.

$$3Fe^{2+} + MnO_4^- + 4H^+ = 3Fe^{3+} + MnO_2 + 2H_2O \quad (1)$$

Table 1

Analytical Methods

The kinetics of phosphate removal by co-precipitation during coagulation and by adsorption after the flocs were formed without phosphate were examined; details are shown in Text S3. The molybdenum blue method invented by Allen Gee et al. was used to detect the phosphate remaining in the water after filtration (0.45 μm membrane filter) using an ultraviolet-visible spectrophotometer (UV-2600, Shimadzu, Japan).[17]

Zeta potential during the coagulation process was measured by a zeta instrument (Nano ZS90, Malvern Inc., UK). The coagulated solution was filtered by a 0.45 μm membrane to remove formed flocs for subsequent DOM analysis. A TOC analyzer (TOC-VCPH, Shimadzu, Japan) was used to determine the total organic carbon. The excitation-emission matrix (EEM) datasets were collected by a Fluorescence spectrophotometer (F-4600, HITACHI, Japan) with a 150 W xenon lamp and analyzed by Parallel factor analysis (PARAFAC) in MATLAB (Text S4).[18] The Molecular weight distribution of the ultraviolet-sensitive substances in solution was determined by size exclusion chromatography (SEC) employing a Waters HPLC system (Waters, United States) with Security Guard™ Cartridges and SEC column (Phenomenex, BioSep μm, s3000, 290 Å).

Floc samples were filtered and freeze-dried to obtain a powdered solid. The characteristic crystal information of flocs was obtained by X-ray diffractometer (XRD, D8 ADVANCE, Germany). The functional groups of substances in filtered and freeze-dried samples were obtained by Fourier Transform infrared spectroscopy (FTIR, NICOLET-8700, Thermo Fisher Scientific, America), normalized with the sum of the measured area, and analyzed by two-dimensional correlation spectroscopy (2D-COS); details are given in Text S5.[19] X-ray photoelectron spectroscopy (XPS, PHI Quantera II, ULVAC, Japan) was used to estimate elemental composition and valence. A transmission electron microscope (TEM, G2 F30 S-TWIN, FEI Tecnai, USA) with an energy-dispersive X-ray spectrometer (EDS) was employed for structural analysis together with DigitalMicrograph and Diamond 3.2 software. The particle size was determined by the image analysis software ImageJ (National Institutes of Health).

EXAFS Experiment and Data Processing

The floc samples were freeze-dried, pressed into pellets, and sealed in a vacuum bag for signal detection. Iron oxidation state and speciation in selected samples were analyzed by bulk Fe K-edge (7112 eV) X-ray absorption spectroscopy (XAS) at Sector 20 BM of the Advanced Photon Source (APS, Argonne, USA). The pre-edge step size was 5 eV, and the edge region was scanned with 0.5 eV steps. The pre-edge and post-edge information of samples and Fe-foil were collected simultaneously to correct for slight energy offsets. Three scans were collected for each sample and averaged. The obtained data was preliminarily processed by Athena software (energy shift, background removal, and normalization),[20] and the Fe-foil reference data detected simultaneously for each sample was used as the basis for energy shift, $K_{weight} = 2$, and $R_{bkg} = 1$, and E0 was defined as zero-crossing in the second XANES derivative of the sample. Linear combination fitting was performed using k^3-weighted EXAFS spectra in the range of k = 2 - 12.15 $Å^{-1}$ for both experimental samples and reference minerals. Reference mineral data were used as a fitting reference, constrained to make the sum of all fractional proportions equal 100%. The E0 of the reference minerals involved in the fitting was set to 7128 eV. More details are provided in our previous study.[21]

The Fortran-based HAMA code was used for the wavelet transform (WT) analysis of k^3-weighted EXAFS spectra; details are given in Text S6. We selected data between R + ΔR (Fe) = 2.0 and 4.0 Å for qualitative research and adjusted the resolution of the signal by changing the values of parameters n and σ to distinguish the contributions of different atoms at different positions. Shell fitting of k3-weighted EXAFS spectra was performed in R-space by Artemis and conducted by nonlinear fitting to the data with the processing k range of 2 - 12.15 $Å^{-1}$ and R range of 1 - 3.5 Å. The ab initio FEFF6 code was used to calculate amplitude functions.

3. Results

Effectiveness of coagulants for phosphate removal

Figure S2a and Text S3 illustrate the effectiveness of various coagulation processes in removing phosphate. The findings indicate that ex-situ Fe(III) is not a suitable option for phosphate removal, as it resulted in 0.64 mg/L of residual phosphate after coagulation. In contrast, Fe(II) coagulants exhibit a high degree of phosphate removal but require a longer reaction time. The in-situ Fe(III) produced by the accelerated oxidation of $KMnO_4$ offered a shorter phosphate removal time while maintaining a high removal rate, surpassing the performance of conventional coagulants. The total phosphorus after coagulation was 0.13 mg/L, less than 0.20 mg/L required by the Chinese government for third-class surface water quality.[22] The disparities in phosphate adsorption depicted in Figure S2c revealed that in-situ Fe(III) created from Fe(II) without $KMnO_4$ exhibited poor phosphate adsorption capacity, while ex-situ Fe(III) displayed strong phosphate adsorption. This indicated that Fe(II) coagulation primarily eliminated phosphate via co-precipitation, whereas phosphorus removal effectiveness by ex-situ Fe(III) was curtailed by the presence of phosphate during co-precipitation. The flocs resulting from the Fe(II)-$KMnO_4$ possess exhibit advantages in both phosphorus adsorption and co-precipitation.

Different Flocs Formed by In-situ and Ex-situ Fe(III)

The real-time growth process of flocs was detected by PDA.[23] Figures 1a and 1b show the growth process of flocs formed by different coagulants with and without phosphate. Due to the natural oxidation by dissolved oxygen, Fe^{2+} slowly formed large agglomerated flocs, while the equilibrium flocculation index (FI) decreased from 4.04% to 2.36% due to the significant

inhibition by phosphate. As the concentration of $KMnO_4$ increased in systems with and without phosphate, the time to reach equilibrium was significantly reduced, and the FI at equilibrium first decreased to 0.43% and 0.90% and then rose to 2.24% and 2.87%, respectively (Figure S3). This showed that adding a low concentration of $KMnO_4$ (Fe(II): Mn=1:0.16) reduced the diameter of formed flocs until they were similar in size to those of ex-situ Fe(III), while a high concentration of $KMnO_4$ promoted floc formation. In addition, the regrowth ability of flocs was also inhibited by $KMnO_4$ because of the decrease of active regions of floc surface.[24]

Figure 1

XRD analysis confirmed that flocs produced by the oxidation of Fe^{2+} in raw water without phosphate were likely lepidocrocite, similar to that found in our previous study.[25] Flocs formed in phosphate-containing water formed a broad peak around $\Theta = 21.5°$, which was evidence of Fe-phosphate co-precipitation formation (Figure S4).[26] We believed that flocs formed by Fe^{2+} without $KMnO_4$ still existed in a possible structure of lepidocrocite, to a slight degree, according to the micro-peak at around $\Theta = 60°$.[27]

TEM analysis further confirmed the above conclusion, where the results showed that there were still sheet-like structures in the Fe(II) flocs, indicating that DOM in natural surface water alone did not have a very obvious inhibitory effect on crystallinity (Figure S5a), and flocs were able to form γ-FeOOH with a certain degree of crystallinity (Figure S6a), which was due to the slow natural oxidation of oxygen and the charge transfer between Fe^{2+} and Fe^{3+}.[28] However, the growth of nanoparticles was substantially inhibited by phosphate, and nanoparticles could not form a sheet-like structure but only existed as spherical colloids, which was consistent with the results observed by Voegelin.[12] This indicated the co-precipitation of

amorphous structures after the slow oxidation of the Fe(II) coagulant. ImageJ software was used to count the average size of particles under the TEM lens: compared with the ex-situ Fe(III) in which Fe^{3+} was directly added, spherical particles formed by Fe^{2+} oxidation had a larger diameter, with an average particle size of 60 nm to 70 nm. As the $KMnO_4$ concentration increased, the diameter of nanoparticles decreased sharply (Figure 1c). Only amorphous substances could be observed in the HRTEM results for the ex-situ Fe(III) and in-situ Fe(III) without $KMnO_4$ control groups when phosphate was added.[29] Combining the XRD results and diffraction rings, it was inferred that both of them form Fe-phosphate amorphous nanoparticles. The addition of $KMnO_4$ to the coagulation system produced many short-range ordered and non-directional lattice fringes in amorphous spheres due to the formation of nanoscale manganese dioxide. With lattice fringes, the structure was judged to be birnessite (δ-MnO_2).[30] Despite the formation of larger crystalline manganese dioxide nanoparticles with increasing $KMnO_4$ concentration, amorphous Fe-phosphate co-precipitates always encapsulated them, resulting in no obvious peaks in the XRD results.

The size distribution of the microscopic nanoparticles alone was insufficient to explain the variation of the macroscopic floc size, and the surface charge was further considered.[31] For flocs formed by adding different coagulants, their surface zeta potentials increased with the ratio of added $KMnO_4$ (from -10.37 mV and -8.02 mV to -5.77 mV and -5.34 mV for phosphate-containing water and phosphate-free water, respectively) (Figure 1d). Combined with the calculation results of DLVO theory given in Text S7, we found that adding $KMnO_4$ could compress the electric double layer, making surface charge more conducive to agglomeration (Figure S7). Factors such as surface potential, nanoparticle diameter, particle

morphology, and particle aspect ratios could dictate the macroscopic size of formed flocs. On the one hand, adding $KMnO_4$ caused the rapid hydrolysis of Fe^{2+} to form low-diameter nanoparticles similar to Fe^{3+}, resulting in a rapid decrease in the FI index. On the other hand, the increase of $KMnO_4$ reduced the negative zeta potential and toward electric charge neutralization, which enhanced the effect of nanoparticle agglomeration. At a high concentration of added $KMnO_4$, most of the Fe(II) was oxidized, and the diameter of nanoparticles was similar to that formed directly by adding Fe^{3+} coagulant. Therefore, the agglomeration ability became the dominant factor affecting the macroscopic floc size. This may explain the phenomenon that the FI value first decreased and then increased as the $KMnO_4$ ratio increased. This combined effect explained the advantage of in-situ Fe(III) as the pretreatment for ultrafiltration. Despite the smaller nanoparticles, in-situ Fe(III) was more likely to agglomerate to larger flocs and thus caused less membrane fouling because of forming a more porous and thinner cake layer.[32]

Selective Removal of DOM by In-situ and Ex-situ Fe(III)

An important objective of coagulation is to remove DOM in water as a key stage of water treatment. We examined the removal of DOM using various coagulation strategies by analysis of water samples before and after treatment. The 3D-EEM analysis was employed here to show the removal of fluorescent substances by coagulation. Using OpenFluor matches listed in Table S1, PARAFAC analysis reveals three primary DOM components, as shown in Figures 2 and S9.[33] Dissolved, hydrophilic, small molecular weight organics represented by the C1 (fulvic-like) component were the main substances in the raw water. Compared with humic-like substances, whose molecular weight ranges from 2000 Daltons to 10000 Daltons, fulvic-like substances have a lower molecular weight (below 2000 Daltons) and a lower carbon-to-oxygen ratio, corresponding to a higher percentage of hydroxyl and carboxyl groups.[34] The primary removal mode of C1 substances was by Fe-natural organic matter (NOM) co-precipitation, while C2 (humic-like) substances were mainly removed by physical processes such as adsorption.[35] For the same coagulant, the presence of phosphate inhibited the removal of NOM, especially for C1, which was likely due to the competition between phosphate and low-molecular-weight organics: Fe combined with phosphate to form Fe-P co-precipitation substances, thereby suppressing the formation of Fe-NOM co-precipitation.[36] C2 removal was also decreased with the addition of phosphate, and this could be attributed to the charge effects. However, the addition of $KMnO_4$ overcame the inhibitory effect of phosphate; that is, the destruction and removal efficiency of fluorescent components for the Fe(II)-$KMnO_4$ system (Fe: Mn =1:0.5) was greater than that for ex-situ Fe(III) in the presence of phosphate. In addition, the C3 (protein-like) component decreased with the increasing $KMnO_4$ ratio because

of the oxidation of excess $KMnO_4$ (Figures 2g~i).

The TOC results showed that the coagulation removal efficiency was complicated because the main components in the raw water were hydrophilic organics (Figure 2c). In the absence of $KMnO_4$, Fe(II) coagulant alone showed poor DOM removal due to the formation of highly crystalline minerals rather than amorphous co-precipitation. As the proportion of $KMnO_4$ increased, the crystalline substances decreased, and their DOM removal ability also increased.[16] Nonetheless, the ex-situ Fe(III) was strongly hindered in removing DOM by the presence of phosphate, while the in-situ Fe(III) produced through $KMnO_4$ was less affected by this phenomenon. The study of Laszakovits et al. showed that adding $KMnO_4$ alone could only reduce the UV_{254} value by changing the structure of NOM without reducing the TOC or causing the mineralization of organics to CO_2.[37] Therefore, the variation of TOC was mainly due to the coagulation.

The Fe(II)-$KMnO_4$ process substantially improved the removal of UV-responsive substances in the solution (Figure S8); as the $KMnO_4$ ratio increased, the UV_{254} removal rose from 49% to 82%, which was greater than the control group (direct addition of Fe^{3+}) (23%). Sample analysis by SEC can reveal the molecular weight distribution of organics in solution. The control group showed that the main components of the pre-treated water were humic acid and medium-sized substances (Figures 2a~b). For these components, adding Fe(II) or Fe(III) coagulant alone removes substances with a molecular weight between 3600 and 2700 Daltons. The addition of $KMnO_4$ not only increased the removal of substances between 3600 and 2700 Daltons but also increased the removal of substances between 1000 and 500 Daltons. This was attributed to the oxidation of the double bonds and phenol ring by $KMnO_4$, making it easier to

292 form co-precipitates with flocs.[38]

293 In summary, the competitive precipitation between Fe-phosphate and Fe-NOM
294 substantially hindered the removal of NOM, especially for the C1 component and medium-
295 molecular-weight substances, when using ex-situ Fe(III) coagulant to treat phosphate-
296 containing water. However, in-situ Fe(III), formed by the Fe(II)-$KMnO_4$ system, appeared to
297 overcome this inhibition, as manifested mainly by the enhanced removal of C1 species and
298 UV_{254} absorbing substances with different molecular weights. This beneficial effect was more
299 pronounced as the ratio of $KMnO_4$ added increased.

300 Figure 2

301

Different Bonding Models Between In-situ and Ex-situ Fe(III) to NOM and Phosphate

FTIR results showed the binding modes of NOM and phosphate in flocs (Figure 3). Three main peak positions were observed: 3300 cm^{-1}, which corresponds to the -OH vibration and represents the contribution of absorbed water and organic hydroxyl groups; the range from 2000 cm^{-1} to 1200 cm^{-1}, which corresponds to the carbon vibration of the carboxyl group bond; and the contribution of phosphate located around 1200 cm^{-1} to 800 cm^{-1}. Specifically, the vibration at 1630 cm^{-1} arises from the bound water in flocs, while 1500 cm^{-1} and 1391 cm^{-1} peaks result from the v_3C-O stretching modes of an adsorbed carboxyl group, representing the asymmetric (vC-O asym) stretch and symmetric (vC-O sym) stretch, respectively.[39] The Fe(II) control group exhibits a strong peak at 1600 cm^{-1}, corresponding to surface-bound or structured water in the amorphous iron phosphate complex.[12] In contrast, flocs formed by the slow oxidation of Fe^{2+} showed only one peak at 1460 cm-1, which suggested that they were mainly combined with NOM by creating outer-sphere sorption with carboxyl groups.[40]

As the ratio of added $KMnO_4$ increased, the peak at 1460 cm^{-1} gradually shifted and divided into two at 1500 cm^{-1} and 1391 cm^{-1}, indicating that the combination between flocs and carboxyl groups gradually tended to that of the Fe(III) control group and changed from outer-sphere sorption to inner-sphere sorption.[41, 42] This change was attributed to the increased incorporation of carboxyl groups into the solid phase through oxidation and precipitation by $KMnO_4$ (Figure 3b). The binding mode of carboxyl groups on flocs was determined by the distance between the asymmetric and symmetrical vibration, ΔV, which proved these groups were mainly chelated bidentate complexes.[43, 44] The slight enhancement at 1600 cm^{-1} might

have arisen from the bidentate adsorption of ethyl acetate, with almost no nitrogen content (Figure S11).[43, 45] In the inner-sphere complexes, binary combinations of both acetate and ethyl acetate forms existed, and the acetate form adsorbed in a higher proportion than the acetate form.

XPS was used to analyze the composition and the proportion of elements in floc samples. The results showed peaks concentrated around 284.6 eV, 285.9 eV, and 288.1 eV, representing C-C/C-H bonds in hydrocarbon compounds, C-O/C-O-C bonds in carbonyl groups, and C=O/O-C-O bonds in carboxyl-containing substances, respectively (Figure S12). The primary forms of organics were aromatic carbon, α-carbon, and carboxyl carbon in flocs.[46 47] From Fe: C ratio, we can deduce that the ability of unit Fe atoms to bind C atoms was in the following order of increasing strength: Fe(II) < Fe(III) < Fe: Mn = 1:0.16 < Fe: Mn = 1:0.33 (Table S2). The proportion of α-carbon and carboxyl carbon in the Fe(II) control group was at a low level of 25.8% and 4.5%, respectively, indicating that fewer NOM were bound to flocs through carboxyl groups. As the dose of $KMnO_4$ increased, the proportion of O-C-O and C=O groups increased, as shown in FTIR results, proving that the increase in the $KMnO_4$ dose indeed strengthened the binding of organics to flocs through carboxyl groups. In addition, the residual Fe(II) decreased as the $KMnO_4$ dose increased, causing its peak position to shift to lower energy until it approached the Fe(III) control group (Figure S12). [12, 48]

In conclusion, the introduction of $KMnO_4$ enhanced the combination between flocs and NOM by changing the binding mode of carboxyl groups, accelerating the oxidation rate of Fe^{2+}. This resulted in more amorphous formed particles and more stable bonding sites for organics. Studies have also shown that $KMnO_4$ can oxidize DOM in water, transform carbonyl into

carboxyl groups, and increase the ratio of C=O double bonds, thus contributing to their removal by coagulation.[37]

The data in the range from 1200 cm^{-1} to 800 cm^{-1} were normalized by dividing the integral area, allowing for a comparison of the proportion of different phosphate forms in flocs (Figures 3c and 3f).[49] Results showed that both monodentate and bidentate phosphates were present in all flocs, regardless of co-precipitation or adsorption. Compared with flocs formed by $FeSO_4$, the peaks in the ex-situ Fe(III) control group shifted to a lower wavenumber and showed lower contributions at 1127 cm^{-1} and 1010 cm^{-1}, indicating that the binding mode of phosphate in flocs tended towards bidentate complexation. Furthermore, flocs that formed first and then adsorbed phosphate exhibited a higher proportion of monodentate adsorption, as evident in the Fe(II) control group, as opposed to co-precipitation (Figure 3c).

According to the 2D-COS FTIR results, the interaction mode between phosphate and flocs was altered as the amount of $KMnO_4$ was increased. Five response peaks were detected in the synchronization diagram at 1127 cm^{-1}, 920 cm^{-1}, 838 cm^{-1}, 1010 cm^{-1}, and 1061 cm^{-1} (Figure 3d), which represented the v(P=O) stretching vibrations, symmetrical vs(P-OFe) stretching vibrations, v(P-OH)B2 vibrations, asymmetrical vas(P-$(OFe)_2$) stretching vibrations, and v(P-O)B1 vibrations, respectively.[50] For co-precipitation, the order of intensities at the diagonal in the synchronization results was 920 cm^{-1} > 1010 cm^{-1} > 838 cm^{-1} > 1127 cm^{-1} > 1061 cm^{-1}, reflecting the sensitivity of the response to the varying proportion of $KMnO_4$. The correlation between peaks showed that the proportion of bidentate and protonated phosphate also increased as $KMnO_4$ increased. The asynchronous results showed that with the increase in $KMnO_4$ ratio, the response sequence of the phosphate peak was 1127 cm^{-1} > 920 cm^{-1} > 838 cm^{-1} > 1010 cm^{-}

^{1} > 1061 cm^{-1}, indicating that the increase of bidentate was more sensitive to the variables, and $KMnO_4$ could enhance the formation of bidentate complexes. For adsorption, according to Noda's rules, the sequence of peaks should decrease in the following sequence: 1010 cm^{-1} > 890 cm^{-1} > 991 cm^{-1} > 920 cm^{-1} > 1061 cm^{-1} > 961 cm^{-1} > 1150 cm^{-1}.[51] This indicated that as $KMnO_4$ was added, more protonated phosphate was adsorbed on the surface through bidentate coordination and the decrease of monodentate adsorption was more sensitive to the dose of $KMnO_4$. This result suggested that $KMnO_4$ enhanced the binding of phosphate to FeOOH by forming a higher proportion of bidentate complexes. However, the FTIR results could not adequately explain the advantage of in-situ Fe(III) over ex-situ Fe(III) because the contribution of co-precipitation was not clearly defined.

EDS analysis showed that the flocs formed by $FeSO_4$ directly had the weakest binding ability for organics, while the ex-situ Fe(III) group had the weakest binding ability for phosphate. Flocs formed by Fe(II)-$KMnO_4$ strengthened the binding ability of both substances (Figure S15). [15] The in-situ Fe(III) had a higher Fe content because of more dense spherical particles (Figure S16, Table S3).

Figure 3

EXAFS Shows Different Coordination Environments of Fe Atoms

EXAFS allowed us to examine the coordination environment of Fe atoms within flocs. The WT distinguished different elements coordinating with Fe and corresponded well with the calculated theoretical backscattering path (Figure 4). The WT analysis of standard mineral structures is illustrated in Text S8. The results of floc samples could be regarded as the superposition of several reference mineral maps. The signal at k = 3.5 $Å^{-1}$ appeared in all four samples, and there was a significant extension, indicating that PO_4 tetrahedra existed in the second shell of these samples. The peak at k = 6.4 $Å^{-1}$, R = 2.75 Å meant that these four samples all contain edge-sharing Fe in the second shell. A clear response at k = 7 $Å^{-1}$, R = 3.5 Å was observed only in the Fe(II) and Fe(III) control groups, proving these two samples contained corner-sharing Fe. However, this signal in flocs formed by $KMnO_4$ extended less backward in the R direction.

It is important to note that all floc samples were analyzed in the same EXAFS synchrotron facility, and their data was processed in a consistent manner. According to the synchrotron radiation formula (Text S6), the peak intensities of these samples in WT could be compared to reveal the average coordination number of atoms at different positions.[52 53 54] The relative peak intensity at k = 7 $Å^{-1}$ and R = 2.75 Å showed that flocs formed in $FeSO_4$ without $KMnO_4$ had a higher intensity than Fe(II): Mn =1:0.16, which in turn had a higher intensity than ex-situ Fe(III) and Fe(II): Mn = 1:0.33. This indicated that in-situ Fe(III) combined more Fe atoms in the second shell than ex-situ Fe(III), resulting in a higher proportion of Fe-Fe coordination. As the $KMnO_4$ ratio increased, the intensity of Fe signal decreased sharply. The proportion of edge-sharing Fe in flocs formed by Fe^{2+} oxidized with a high $KMnO_4$ concentration was even

lower than that of flocs formed directly by Fe^{3+}. The intensity of the signal at k = 3.5 $Å^{-1}$ represents the coordination relationship between Fe and P; among these four samples, only the ex-situ Fe(III) control group had a significant decrease in the radial direction, indicating that the coordination number of the Fe-P bond in this sample was lower than others.

Figure 4

Fe K-edge XANES spectrum showed that the highest peak signals of four floc samples were concentrated around 7131 eV, similar to the reference ferrihydrite and strengite, indicating that Fe mainly existed in the trivalent form (Figure 5d). The Fe peak shifted slightly to lower energy in flocs formed by Fe(II) slow oxidation. The signal at 7129 eV indicated that there was still a small amount of unoxidized Fe(II) in the solid phase formed by Fe(II), which is consistent with XPS results.

From WT results, four standard substances were selected as references to perform linear fitting on floc samples (Table S4). Results showed that the major components were ferrihydrite and strengite. In the Fe(III) control group, ferrihydrite represented the main phase (62.4%), followed by strengite (37.7%). For Fe(II): Mn=1:0, their fractions were 18.7% and 62.7%, respectively. This indicated that more amorphous ferric phosphate was formed in flocs formed by Fe^{2+} oxidation. The proportion of strengite in $KMnO_4$-Fe(II) systems was higher than that of ex-situ Fe(III) and similar to Fe(II) without $KMnO_4$, indicating that the presence of oxidants did not interfere with the strong binding of in-situ Fe(III) to phosphate. In addition, the signals of high-crystallinity minerals (lepidocrocite, goethite) were fitted in Fe(II) without KMnO4, and vivianite species only appeared in this sample, explaining the energy shift of XANES. The linear fitting results showed that the addition of $KMnO_4$ destroyed the formation of minerals

429 with high crystallinity in the Fe^{2+} oxidation process but still retained a high proportion of
430 amorphous Fe-phosphate co-precipitation, which is similar to strengite in structure, compared
431 with that formed by ex-situ Fe(III).

432 We also performed a shell-fitting analysis for the first three shells of Fe EXAFS data to
433 explore its local coordination environment (Figure 5 and Table S5). To reduce the variables,
434 we assumed that the central Fe atom formed FeO_6 octahedral in the first shell and fixed the σ
435 parameter of each layer. Therefore, the Fe-O path with a bond length of 1.99 Å was chosen,
436 and the coordination number of the first-layer Fe-O bond was considered as per the model by
437 Michel et al.[55] According to the previous analysis, we represented the expected path of the
438 corner-sharing phosphate tetrahedron in amorphous iron phosphate using the Fe-P path of R =
439 3.28 Å of strengite.[11] The Fe-Fe_1 pathway with R=3.06 Å and the Fe-Fe_2 pathway with R =
440 3.48 Å represented the contribution of edge-sharing and corner-sharing Fe, respectively.

441 Results showed that the coordination number of flocs was lower than that of ferrihydrite
442 in Fe-Fe_1 and Fe-Fe_2 because of the inhabitation of PO_4 tetrahedrons. The flocs formed by the
443 slow oxidation of Fe^{2+} retained a higher coordination number in the second shell than the ex-
444 situ Fe(III) formed by adding Fe^{3+} directly. With more edge-sharing and corner-sharing Fe, the
445 Fe(II) control group formed more edge-sharing dimers and trimers. There is a higher possibility
446 of forming chains and the semi-local structure composed of FeO_6 octahedra, resulting in larger
447 nanoparticles of flocs.[56] With the introduction of $KMnO_4$, the oxidation of Fe^{2+} was accelerated,
448 resulting in faster precipitation. As a consequence, the contribution of edge-sharing Fe dropped
449 rapidly, and no corner-sharing Fe could be evidenced. This suggested that trimers were unlikely
450 to exist in these samples. Increasing $KMnO_4$ further inhibits the formation of edge-sharing Fe

by limiting hydrolysis and thus impedes the production of dimeric FeO_6. The above shell-fitting hypothesis can well explain the results of nanoparticles in TEM: the coordination number of edge-sharing and corner-sharing Fe in different flocs caused the change in the polymerization morphology of the FeO_6 octahedron, the size, and the morphology of particles. In-situ Fe(III) formed larger monomer nano-sized multimers due to the contribution of more edge-coordinated and corner-coordinated Fe. With the rapid oxidation of $KMnO_4$, only multinuclear Fe(III) oxyhydroxide clusters dominated by oligomers were formed, which had a lower coordination number than ex-situ Fe(III), and led to less aggregation and smaller nanoparticles.

The analysis of the Fe-P pathway showed that amorphous ferric phosphate was formed in these four samples and exhibited a strengite-like structure. The P atoms were coordinated with Fe in the second shell, combined with FeO_6 octahedra through PO_4 tetrahedra. The shell fitting results showed that the second shell of Fe in the Fe(II) control group had more phosphorus atoms coordinated than that in the Fe(III) control group. Increasing the proportion of $KMnO_4$ led to a slight decrease in the average Fe-phosphorus coordination number. However, its number of bound phosphorus atoms was still greater than that of ex-situ Fe(III). This result proved that in-situ Fe(III) could form more angle-coordinated phosphates than ex-situ Fe(III) and explains why the Fe(II)-$KMnO_4$ coagulant is superior to Fe(III) in the removal of phosphates.

Figure 5

4. Environmental Implications

The prevention of excess phosphate in water bodies continues to be a significant environmental challenge. In this study, we have presented a novel in-situ Fe(III) coagulation process through the oxidation of Fe^{2+} with $KMnO_4$ that can treat surface water containing phosphate more effectively compared to ex-situ Fe(III) in phosphate and DOM removal. Furthermore, our study offers in-depth insights into fundamental mechanisms responsible for the superiority of in-situ Fe(III) in coagulation-based phosphate removal, which could inspire the integration of scientific analysis methods with engineering problems. EXAFS helped to successfully explain the structure of amorphous Fe in the Fe-Mn mixed system, which provides ideas for similar studies when facing complex amorphous systems.

More importantly, the findings of this study have critical implications for the field of geochemistry and the Fe cycle in nature. Our results highlight the complex interplay between NOM, Fe, and phosphate, and demonstrate that the oxidation process selectively modifies the coordination environment of Fe in co-precipitates, altering the linking mode between aggregates. By preserving the angular coordination structure relationship between FeO_6 octahedrons and PO_4 tetrahedrons during oxidation, we underscore the crucial role of short-range structure in co-precipitations formed by oxidized Fe^{2+}. Through a better understanding of the structural differences between Fe-P amorphous co-precipitates formed under varying oxidation conditions, we can gain a deeper appreciation of the variations in elemental cycling outcomes. Overall, this study emphasizes the importance of addressing environmental challenges through multidisciplinary approaches that bridge the gap between scientific analysis and practical engineering solutions.

References

(1) Karl, D. M. Aquatic ecology. Phosphorus, the staff of life. *Nature* **2000**, *406* (6791), 31, 33. DOI: 10.1038/35017683.

(2) Jupp, A. R.; Beijer, S.; Narain, G. C.; Schipper, W.; Slootweg, J. C. Phosphorus recovery and recycling - closing the loop. *Chem Soc Rev* **2021**, *50* (1), 87-101. DOI: 10.1039/d0cs01150a.

(3) Cordell, D.; Drangert, J. O.; White, S. The story of phosphorus: Global food security and food for thought. *Global Environ Chang* **2009**, *19* (2), 292-305. DOI: 10.1016/j.gloenvcha.2008.10.009.

(4) Elser, J.; Bennett, E. Phosphorus cycle: A broken biogeochemical cycle. *Nature* **2011**, *478* (7367), 29-31. DOI: 10.1038/478029a.

(5) de-Bashan, L. E.; Bashan, Y. Recent advances in removing phosphorus from wastewater and its future use as fertilizer (1997-2003). *Water Res* **2004**, *38* (19), 4222-4246. DOI: 10.1016/j.watres.2004.07.014.

(6) Wei, H.; Gao, B.; Ren, J.; Li, A.; Yang, H. Coagulation/flocculation in dewatering of sludge: A review. *Water Res* **2018**, *143*, 608-631. DOI: 10.1016/j.watres.2018.07.029.

(7) Liu, B.; Qu, F.; Chen, W.; Liang, H.; Wang, T.; Cheng, X.; Yu, H.; Li, G.; Van der Bruggen, B. Microcystis aeruginosa-laden water treatment using enhanced coagulation by persulfate/Fe(II), ozone and permanganate: Comparison of the simultaneous and successive oxidant dosing strategy. *Water Res* **2017**, *125*, 72-80. DOI: 10.1016/j.watres.2017.08.035. Cheng, X.; Liang, H.; Ding, A.; Tang, X.; Liu, B.; Zhu, X.; Gan, Z.; Wu, D.; Li, G. Ferrous iron/peroxymonosulfate oxidation as a pretreatment for ceramic ultrafiltration membrane: Control of natural organic matter fouling and degradation of atrazine. *Water Res* **2017**, *113*, 32-41. DOI: 10.1016/j.watres.2017.01.055.

(8) Zhang, J.; Bligh, M. W.; Liang, P.; Waite, T. D.; Huang, X. Phosphorus removal by in situ generated Fe(II): Efficacy, kinetics and mechanism. *Water Res* **2018**, *136*, 120-130. DOI: 10.1016/j.watres.2018.02.049. Guan, X.; Ma, J.; Dong, H.; Jiang, L. Removal of arsenic from water: effect of calcium ions on As(III) removal in the KMnO(4)-Fe(II) process. *Water Res* **2009**, *43* (20), 5119-5128. DOI: 10.1016/j.watres.2008.12.054. Lu, J. B.; Hao, J.; Cheng, F.; Liu, H. J.; Qu, J. H. Phosphate Removal from Water Using Novel Fe2+-KMnO4 Process: Significant Role of In Situ-Formed Fe(III). *J Environ Eng* **2015**, *141* (2). DOI: 10.1061/(Asce)Ee.1943-7870.0000881. Liu, X.; Ding, S.; Wang, P.; Hong, Y.; Zhao, H.; Chu, W. Simultaneous mitigation of disinfection by-product formation and odor compounds by peroxide/Fe(II)-based process: Combination of oxidation and coagulation. *Water Res* **2021**, *201*, 117327. DOI: 10.1016/j.watres.2021.117327. Ma, M.; Liu, R.; Liu, H.; Qu, J. Effect of moderate pre-oxidation on the removal of Microcystis aeruginosa by KMnO4-Fe(II) process: significance of the in-situ formed Fe(III). *Water Res* **2012**, *46* (1), 73-81. DOI: 10.1016/j.watres.2011.10.022.

(9) Ma, M.; Liu, R. P.; Liu, H. J.; Qu, J. H. Effect of moderate pre-oxidation on the removal of Microcystis aeruginosa by KMnO4-Fe(II) process: Significance of the in-situ formed Fe(III). *Water Res* **2012**, *46* (1), 73-81. DOI: 10.1016/j.watres.2011.10.022.

(10) Senn, A. C.; Kaegi, R.; Hug, S. J.; Hering, J. G.; Mangold, S.; Voegelin, A. Effect of aging on the structure and phosphate retention of Fe(III)-precipitates formed by Fe(II) oxidation in water. *Geochim Cosmochim Ac* **2017**, *202*, 341-360. DOI: 10.1016/j.gca.2016.12.033.

(11) Mikutta, C.; Schroder, C.; Michel, F. M. Total X-ray scattering, EXAFS, and Mossbauer spectroscopy analyses of amorphous ferric arsenate and amorphous ferric phosphate. *Geochim Cosmochim Ac* **2014**, *140*, 708-719. DOI: 10.1016/j.gca.2014.05.040.

(12) Voegelin, A.; Senn, A. C.; Kaegi, R.; Hug, S. J.; Mangold, S. Dynamic Fe-precipitate formation induced by Fe(II) oxidation in aerated phosphate-containing water. *Geochim Cosmochim Ac* **2013**, *117*, 216-231. DOI: 10.1016/j.gca.2013.04.022.

(13) Voegelin, A.; Kaegi, R.; Frommer, J.; Vantelon, D.; Hug, S. J. Effect of phosphate, silicate, and Ca on Fe(III)-precipitates formed in aerated Fe(II)- and As(III)-containing water studied by X-ray absorption spectroscopy. *Geochim Cosmochim Ac* **2010**, *74* (1), 164-186. DOI: 10.1016/j.gca.2009.09.020.
(14) Senn, A. C.; Hug, S. J.; Kaegi, R.; Hering, J. G.; Voegelin, A. Arsenate co-precipitation with Fe(II) oxidation products and retention or release during precipitate aging. *Water Research* **2018**, *131*, 334-345. DOI: 10.1016/j.watres.2017.12.038.
(15) Senn, A. C.; Kaegi, R.; Hug, S. J.; Hering, J. G.; Mangold, S.; Voegelin, A. Composition and structure of Fe(III)-precipitates formed by Fe(II) oxidation in water at near-neutral pH: Interdependent effects of phosphate, silicate and Ca. *Geochim Cosmochim Ac* **2015**, *162*, 220-246. DOI: 10.1016/j.gca.2015.04.032.
(16) Li, X.; Graham, N. J. D.; Deng, W. S.; Liu, M. J.; Liu, T.; Yu, W. Z. Structural Variation of Precipitates Formed by Fe(II) Oxidation and Impact on the Retention of Phosphate. *Environ Sci Technol* **2022**, *56* (7), 4345-4355. DOI: 10.1021/acs.est.1c06256.
(17) Gee, A.; Deitz, V. R. Determination of Phosphate by Differential Spectrophotometry. *Anal Chem* **1953**, *25* (9), 1320-1324. DOI: DOI 10.1021/ac60081a006.
(18) Stedmon, C. A.; Bro, R. Characterizing dissolved organic matter fluorescence with parallel factor analysis: a tutorial. *Limnol Oceanogr-Meth* **2008**, *6*, 572-579. DOI: DOI 10.4319/lom.2008.6.572.
(19) Hur, J.; Jung, K. Y.; Jung, Y. M. Characterization of spectral responses of humic substances upon UV irradiation using two-dimensional correlation spectroscopy. *Water Research* **2011**, *45* (9), 2965-2974. DOI: 10.1016/j.watres.2011.03.013.
(20) Ravel, B.; Newville, M. ATHENA, ARTEMIS, HEPHAESTUS: data analysis for X-ray absorption spectroscopy using IFEFFIT. *J Synchrotron Radiat* **2005**, *12*, 537-541. DOI: 10.1107/S0909049505012719.
(21) Zhou, Z.; Liu, P.; Wang, S.; Finfrock, Y. Z.; Ye, Z.; Feng, Y.; Li, X. Iron-modified biochar-based bilayer permeable reactive barrier for Cr(VI) removal. *J Hazard Mater* **2022**, *439*, 129636. DOI: 10.1016/j.jhazmat.2022.129636. Ye, Z. H.; Zhou, J. W.; Liao, P.; Finfrock, Z.; Liu, Y. Y.; Shu, C.; Liu, P. Metal (Fe, Cu, and As) transformation and association within secondary minerals in neutralized acid mine drainage characterized using X-ray absorption spectroscopy. *Appl Geochem* **2022**, *139*. DOI: ARTN 105242 10.1016/j.apgeochem.2022.105242.
(22) *Environmental quality standards for surface water*. 2002. (accessed.
(23) Gregory, J. Turbidity Fluctuations in Flowing Suspensions. *J Colloid Interf Sci* **1985**, *105* (2), 357-371. DOI: Doi 10.1016/0021-9797(85)90309-1.
(24) Ghernaout, D.; Ghernaout, B. Sweep flocculation as a second form of charge neutralisation-a review. *Desalin Water Treat* **2012**, *44* (1-3), 15-28. DOI: 10.1080/19443994.2012.691699.
(25) Li, X.; Graham, N. J. D.; Deng, W.; Liu, M.; Liu, T.; Yu, W. The formation of planar crystalline flocs of gamma-FeOOH in Fe(II) coagulation and the influence of humic acid. *Water Res* **2020**, *185*, 116250. DOI: 10.1016/j.watres.2020.116250.
(26) Kandori, K.; Kuwae, T.; Ishikawa, T. Control on size and adsorptive properties of spherical ferric phosphate particles. *J Colloid Interface Sci* **2006**, *300* (1), 225-231. DOI: 10.1016/j.jcis.2006.03.072.
(27) Ahmad, A.; van der Wal, A.; Bhattacharya, P.; van Genuchten, C. M. Characteristics of Fe and Mn bearing precipitates generated by Fe(II) and Mn(II) co-oxidation with O2, MnO4 and HOCl in the presence of groundwater ions. *Water Res* **2019**, *161*, 505-516. DOI: 10.1016/j.watres.2019.06.036.
(28) Li, X.; Graham, N. J. D.; Deng, W.; Liu, M.; Liu, T.; Yu, W. Structural Variation of Precipitates Formed by Fe(II) Oxidation and Impact on the Retention of Phosphate. *Environ Sci Technol* **2022**, *56* (7), 4345-4355. DOI: 10.1021/acs.est.1c06256.
(29) Santoro, V.; Martin, M.; Persson, P.; Lerda, C.; Said-Pullicino, D.; Magnacca, G.; Celi, L. Inorganic and

organic P retention by coprecipitation during ferrous iron oxidation. *Geoderma* **2019**, *348*, 168-180. DOI: 10.1016/j.geoderma.2019.04.004.
(30) Charbonnet, J. A.; Duan, Y.; van Genuchten, C. M.; Sedlak, D. L. Regenerated Manganese-Oxide Coated Sands: The Role of Mineral Phase in Organic Contaminant Reactivity. *Environ Sci Technol* **2021**, *55* (8), 5282-5290. DOI: 10.1021/acs.est.0c05745.
(31) McCurdy, K.; Carlson, K.; Gregory, D. Floc morphology and cyclic shearing recovery: comparison of alum and polyaluminum chloride coagulants. *Water Res* **2004**, *38* (2), 486-494. DOI: 10.1016/j.watres.2003.10.005.
(32) Yu, W. Z.; Liu, T.; Gregory, J.; Campos, L.; Li, G. B.; Qu, J. H. Influence of flocs breakage process on submerged ultrafiltration membrane fouling. *J Membrane Sci* **2011**, *385* (1-2), 194-199. DOI: 10.1016/j.memsci.2011.09.039.
(33) Murphy, K. R.; Stedmon, C. A.; Wenig, P.; Bro, R. OpenFluor- an online spectral library of auto-fluorescence by organic compounds in the environment. *Anal Methods-Uk* **2014**, *6* (3), 658-661. DOI: 10.1039/c3ay41935e.
(34) Sutzkover-Gutman, I.; Hasson, D.; Semiat, R. Humic substances fouling in ultrafiltration processes. *Desalination* **2010**, *261* (3), 218-231. DOI: 10.1016/j.desal.2010.05.008.
(35) Yu, J. J.; Xu, H.; Wang, D. S.; Sun, H. Y.; Jiao, R. Y.; Liu, Y.; Jin, Z. Y.; Zhang, S. Variations in NOM during floc aging: Effect of typical Al-based coagulants and different particle sizes. *Water Research* **2022**, *218*. DOI: ARTN 118486
10.1016/j.watres.2022.118486.
(36) Moens, C.; Smolders, E. Suwannee River Natural Organic Matter concentrations affect the size and phosphate uptake of colloids formed by iron oxidation. *Geochim Cosmochim Ac* **2021**, *312*, 375-391. DOI: 10.1016/j.gca.2021.07.028.
(37) Laszakovits, J. R.; Somogyi, A.; MacKay, A. A. Chemical Alterations of Dissolved Organic Matter by Permanganate Oxidation. *Environ Sci Technol* **2020**, *54* (6), 3256-3266. DOI: 10.1021/acs.est.9b06675.
(38) Laszakovits, J. R.; Somogyi, A.; MacKay, A. A. Chemical Alterations of Dissolved Organic Matter by Permanganate Oxidation. *Environ Sci Technol* **2020**, *54* (6), 3256-3266. DOI: 10.1021/acs.est.9b06675.
(39) Yeasmin, S.; Singh, B.; Kookana, R. S.; Farrell, M.; Sparks, D. L.; Johnston, C. T. Influence of mineral characteristics on the retention of low molecular weight organic compounds: a batch sorption-desorption and ATR-FTIR study. *J Colloid Interface Sci* **2014**, *432*, 246-257. DOI: 10.1016/j.jcis.2014.06.036.
(40) Hausner, D. B.; Bhandari, N.; Pierre-Louis, A. M.; Kubicki, J. D.; Strongin, D. R. Ferrihydrite reactivity toward carbon dioxide. *J Colloid Interface Sci* **2009**, *337* (2), 492-500. DOI: 10.1016/j.jcis.2009.05.069.
(41) Duckworth, O. W.; Martin, S. T. Surface complexation and dissolution of hematite by C-1-C-6 dicarboxylic acids at pH=5.0. *Geochim Cosmochim Ac* **2001**, *65* (23), 4289-4301. DOI: Doi 10.1016/S0016-7037(01)00696-2.
(42) Parikh, S. J.; Mukome, F. N.; Zhang, X. ATR-FTIR spectroscopic evidence for biomolecular phosphorus and carboxyl groups facilitating bacterial adhesion to iron oxides. *Colloids Surf B Biointerfaces* **2014**, *119*, 38-46. DOI: 10.1016/j.colsurfb.2014.04.022.
(43) Gao, X.; Metge, D. W.; Ray, C.; Harvey, R. W.; Chorover, J. Surface complexation of carboxylate adheres Cryptosporidium parvum oocysts to the hematite-water interface. *Environ Sci Technol* **2009**, *43* (19), 7423-7429. DOI: 10.1021/es901346z.
(44) Noren, K.; Persson, P. Adsorption of monocarboxylates at the water/goethite interface: The importance of hydrogen bonding. *Geochim Cosmochim Ac* **2007**, *71* (23), 5717-5730. DOI: 10.1016/j.gca.2007.04.037.
(45) Persson, P.; Karlsson, M.; Ohman, L. O. Coordination of acetate to Al(III) in aqueous solution and at the

water-aluminum hydroxide interface: A potentiometric and attenuated total reflectance FTIR study. *Geochim Cosmochim Ac* **1998**, *62* (23-24), 3657-3668. DOI: Doi 10.1016/S0016-7037(98)00260-9.
(46) Liu, B. B.; Gao, Y.; Pan, J. W.; Feng, Q. Y.; Yue, Q. Y.; Guo, K. Y.; Gao, B. Y. Coagulation behavior of polyaluminum-titanium chloride composite coagulant with humic acid: A mechanism analysis. *Water Research* **2022**, *220*. DOI: ARTN 118633
10.1016/j.watres.2022.118633.
(47) Xiong, X. J.; Bond, T.; Siddique, M. S.; Yu, W. Z. The stimulation of microbial activity by microplastic contributes to membrane fouling in ultrafiltration. *J Membrane Sci* **2021**, *635*. DOI: ARTN 119477
10.1016/j.memsci.2021.119477.
(48) Li, Z. F.; Li, M.; Tan, B.; Du, N.; Zhang, Q.; Li, C. W.; Zhang, Y. B.; Li, J. W.; Li, J. Y. Green rust (GR) and glucose oxidase (GOX) based Fenton-like reaction: Capacity of sustainable release, promoted conversion of glucose through GOX-iron and pH self-adjustment. *Environ Res* **2022**, *208*. DOI: ARTN 112656
10.1016/j.envres.2021.112656.
(49) Xu, H.; Jiang, H. UV-induced photochemical heterogeneity of dissolved and attached organic matter associated with cyanobacterial blooms in a eutrophic freshwater lake. *Water Res* **2013**, *47* (17), 6506-6515. DOI: 10.1016/j.watres.2013.08.021.
(50) Xing, B. B.; Zhao, B. H.; Liu, M. J.; Graham, N. J. D.; Yu, W. Z. The influence of crystal structure and formation path of precursor on phosphate adsorption during oxidation-hydrolysis phase transition of siderite. *Chem Eng J* **2022**, *431*. DOI: ARTN 133358
10.1016/j.cej.2021.133358. Li, X.; Yan, L.; Zhong, W.; Kersten, M.; Jing, C. Competitive arsenate and phosphate adsorption on alpha-FeOOH, LaOOH, and nano-TiO2: Two-dimensional correlation spectroscopy study. *J Hazard Mater* **2021**, *414*, 125512. DOI: 10.1016/j.jhazmat.2021.125512. Yan, W.; Jing, C. Molecular Insights into Glyphosate Adsorption to Goethite Gained from ATR-FTIR, Two-Dimensional Correlation Spectroscopy, and DFT Study. *Environ Sci Technol* **2018**, *52* (4), 1946-1953. DOI: 10.1021/acs.est.7b05643.
(51) Noda, I. Generalized 2-Dimensional Correlation Method Applicable to Infrared, Raman, and Other Types of Spectroscopy. *Appl Spectrosc* **1993**, *47* (9), 1329-1336. DOI: Doi 10.1366/0003702934067694.
(52) Munoz, M.; Argoul, P.; Farges, F. Continuous Cauchy wavelet transform analyses of EXAFS spectra: A qualitative approach. *Am Mineral* **2003**, *88* (4), 694-700. DOI: DOI 10.2138/am-2003-0423.
(53) Aimoz, L.; Taviot-Gueho, C.; Churakov, S. V.; Chukalina, M.; Dahn, R.; Curti, E.; Bordet, P.; Vespa, M. Anion and Cation Order in Iodide-Bearing Mg/Zn-Al Layered Double Hydroxides. *J Phys Chem C* **2012**, *116* (9), 5460-5475. DOI: 10.1021/jp2119636.
(54) Timoshenko, J.; Kuzmin, A. Wavelet data analysis of EXAFS spectra. *Comput Phys Commun* **2009**, *180* (6), 920-925. DOI: 10.1016/j.cpc.2008.12.020.
(55) Michel, F. M.; Ehm, L.; Antao, S. M.; Lee, P. L.; Chupas, P. J.; Liu, G.; Strongin, D. R.; Schoonen, M. A.; Phillips, B. L.; Parise, J. B. The structure of ferrihydrite, a nanocrystalline material. *Science* **2007**, *316* (5832), 1726-1729. DOI: 10.1126/science.1142525.
(56) Lartiges, B.; El Samrani, A. G.; Montarges-Pelletier, E.; Bihannic, I.; Briois, V.; Michot, L. Aggregating ability of ferric chloride in the presence of phosphate ligand. *Water Res* **2019**, *164*, 114960. DOI: 10.1016/j.watres.2019.114960.

Acknowledgments

This work was financially supported by the Key Research and Development Plan of the Chinese Ministry of Science and Technology (No. 2019YFC1906501 and No. 2019YFD1100104) and the Beijing Natural Science Foundation (No. JQ21032).

X-ray absorption spectroscopy analyses were performed at Beamlines 20&9-BM, and 20-ID of the Advanced Photon Source, Argonne National Laboratory.

Associated content

All data needed to evaluate the conclusions in the paper are presented in the paper and/or the Supplementary Materials. Additional data relating to this paper may be requested from the authors.

Author information

Corresponding Author

*E-mail: wzyu@rcees.ac.cn;

ORCID: orcid.org/0000-0001-9776-8021

Notes

The authors declare no competing interests.

687 **Table 1. Principal water quality characteristics of JM water samples.**

	TOC (mg/L)	UV_{254} (AU/cm)	pH	Conductivity (μS/cm)	Ca^{2+} (mg/L)	Mg^{2+} (mg/L)	P (mg/L)	Dissolved oxygen (mg/L)
Jingmi River (JM water)	5.87	0.07	7.12	271	31.9	6.03	0.03	4.34

688

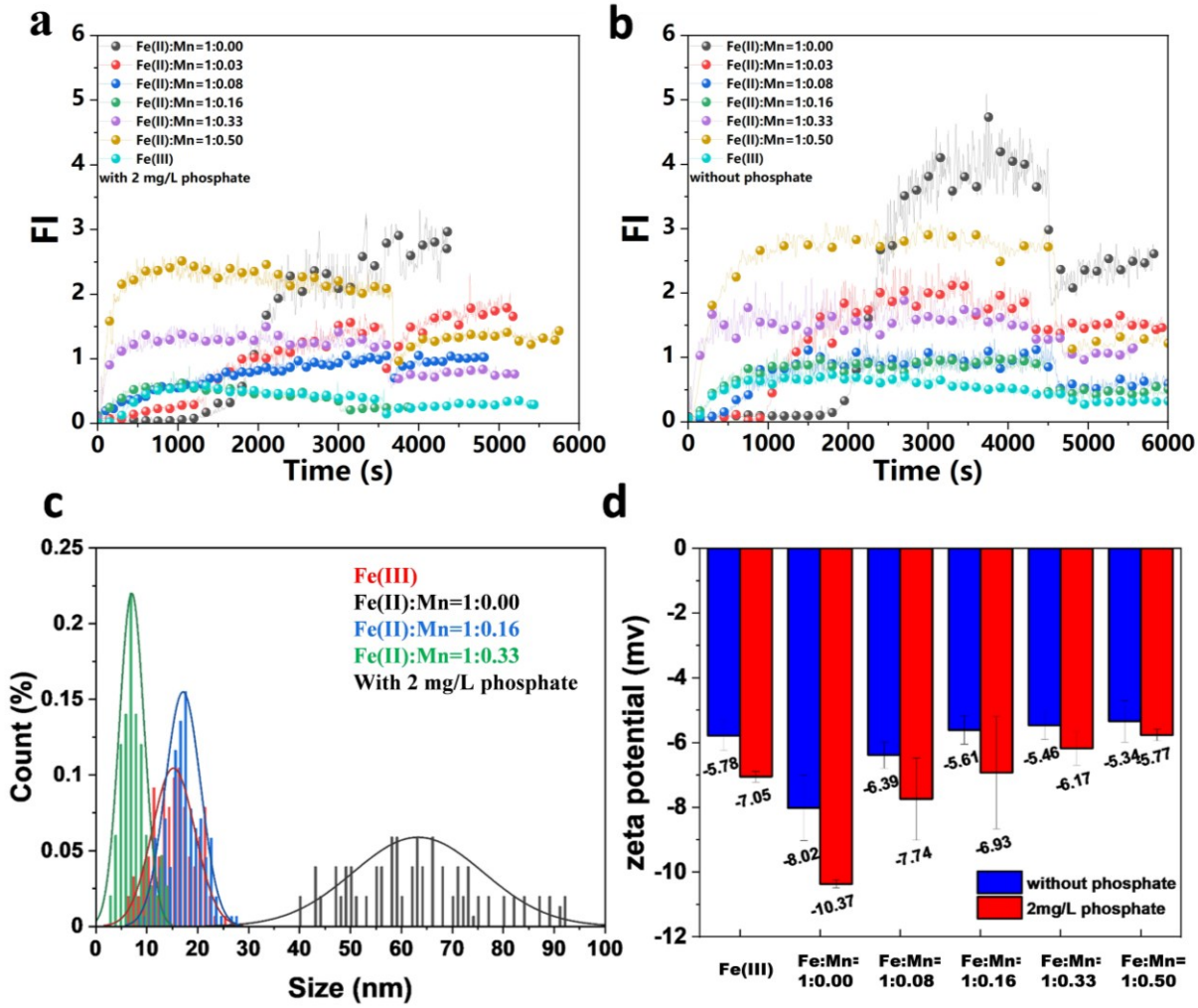

Fig. 1: Coagulation performance and properties of flocs. The variation in flocculation index (FI), before and after floc breakage, for different concentrations of $KMnO_4$ (ratio of Fe(II): Mn shown, at constant 0.2 mmol Fe/L) with (a) or without (b) phosphate in the system. Monomer diameter distribution of different flocs formed with phosphate in TEM results of Figure S5 (c). Zeta potential of different coagulation systems (d).

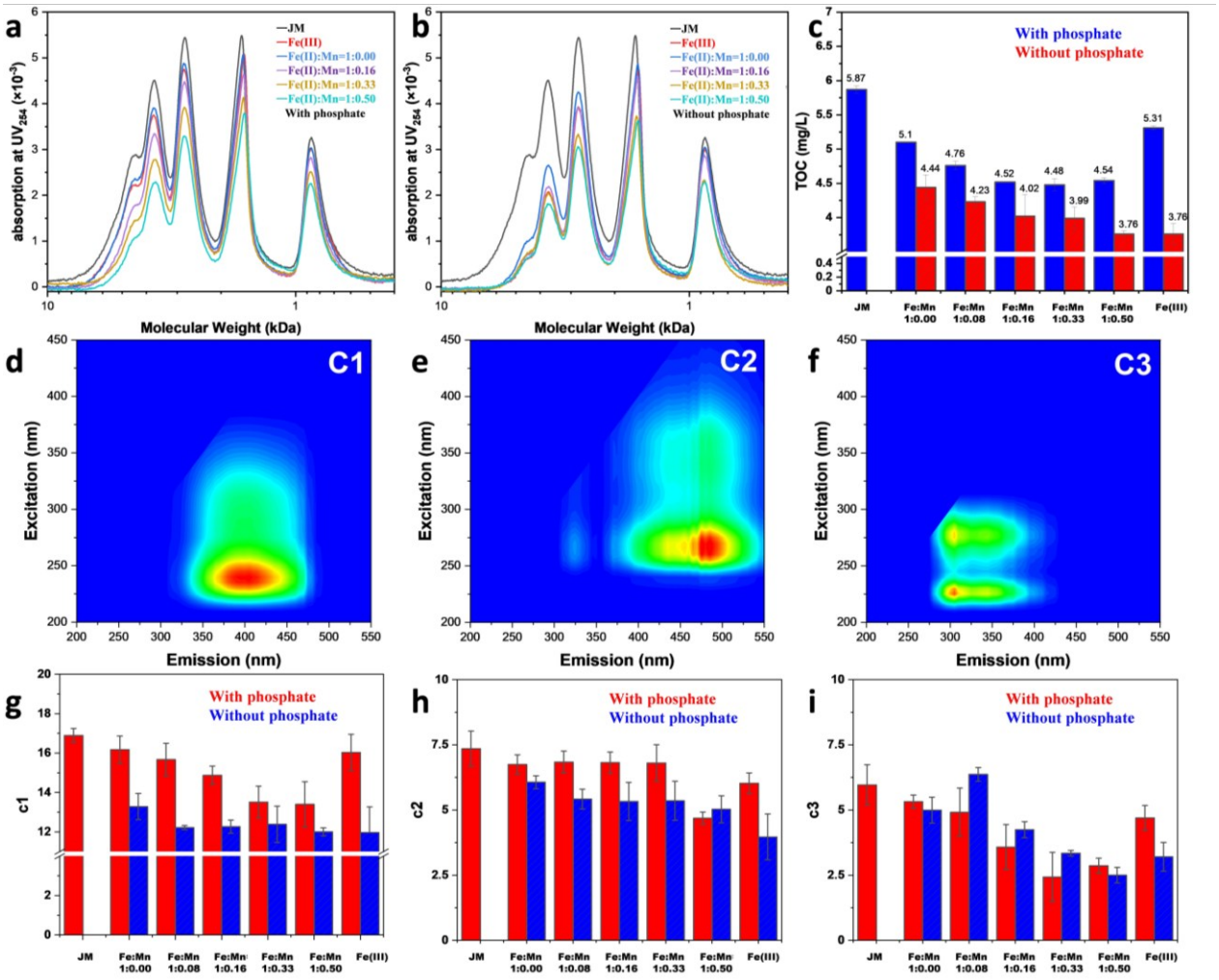

Fig. 2: The molecular weight distributions from SEC of water samples before and after treatment with different coagulants, with (a) and without (b) phosphate. The TOC of water samples before and after treatment with different coagulants with and without phosphate (c). Fmax of PARAFAC model components vs. different coagulants (g~i), and EEM spectra of C1(d), C2(e), and C3(f).

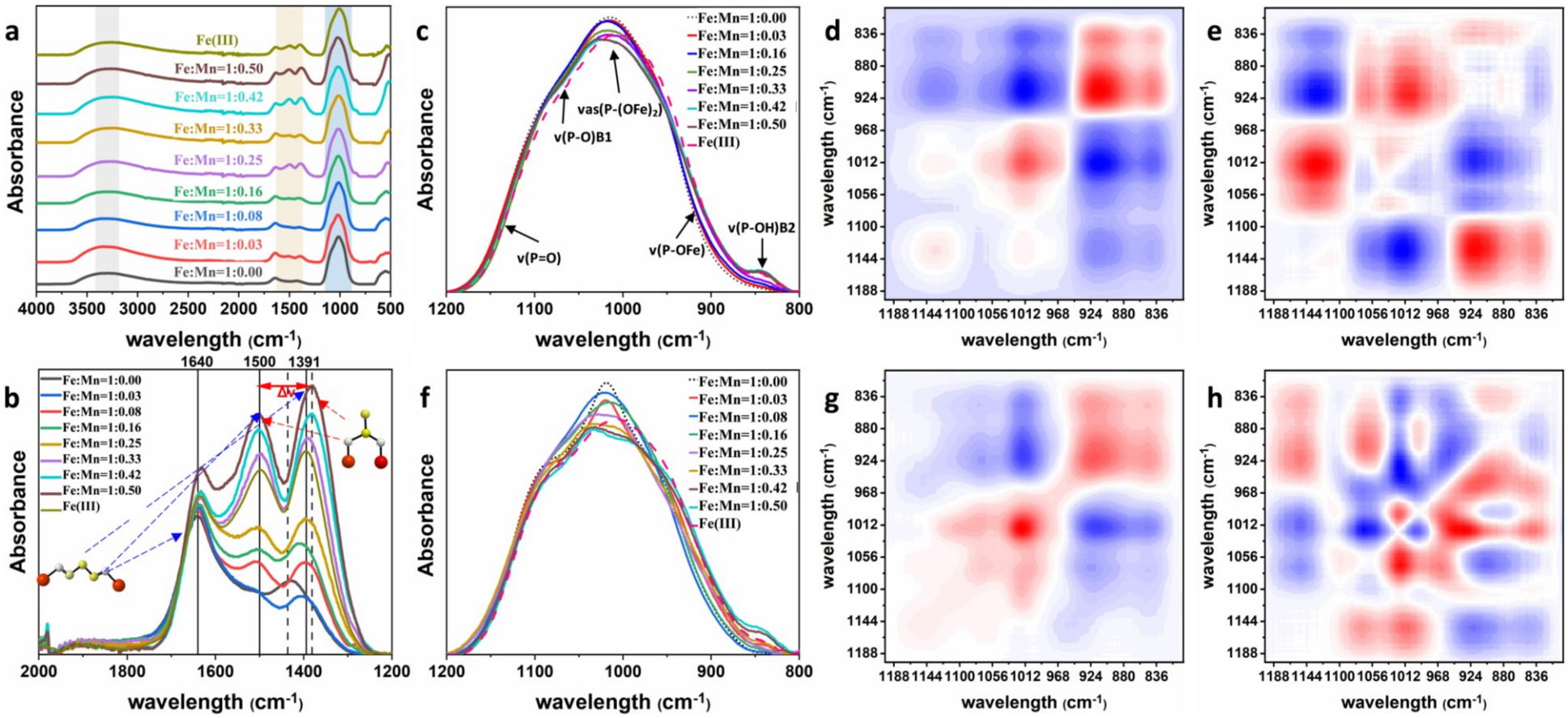

704

705 **Fig. 3: Binding modes of phosphate and organics on flocs through ATR-FTIR analysis.** FTIR data of flocs formed by different coagulants with phosphate
706 (a) and their high-resolution data at 2000-1200 cm^{-1} (b). Normalized spectrum, synchronous and asynchronous FTIR-2D-COS maps of flocs formed with
707 different ratios of $KMnO_4$ by co-precipitation (c~e) or adsorption (f~h) with phosphate. Red represents positive correlations, and blue represents negative
708 correlations; deeper color intensity suggests a stronger positive or negative correlation.

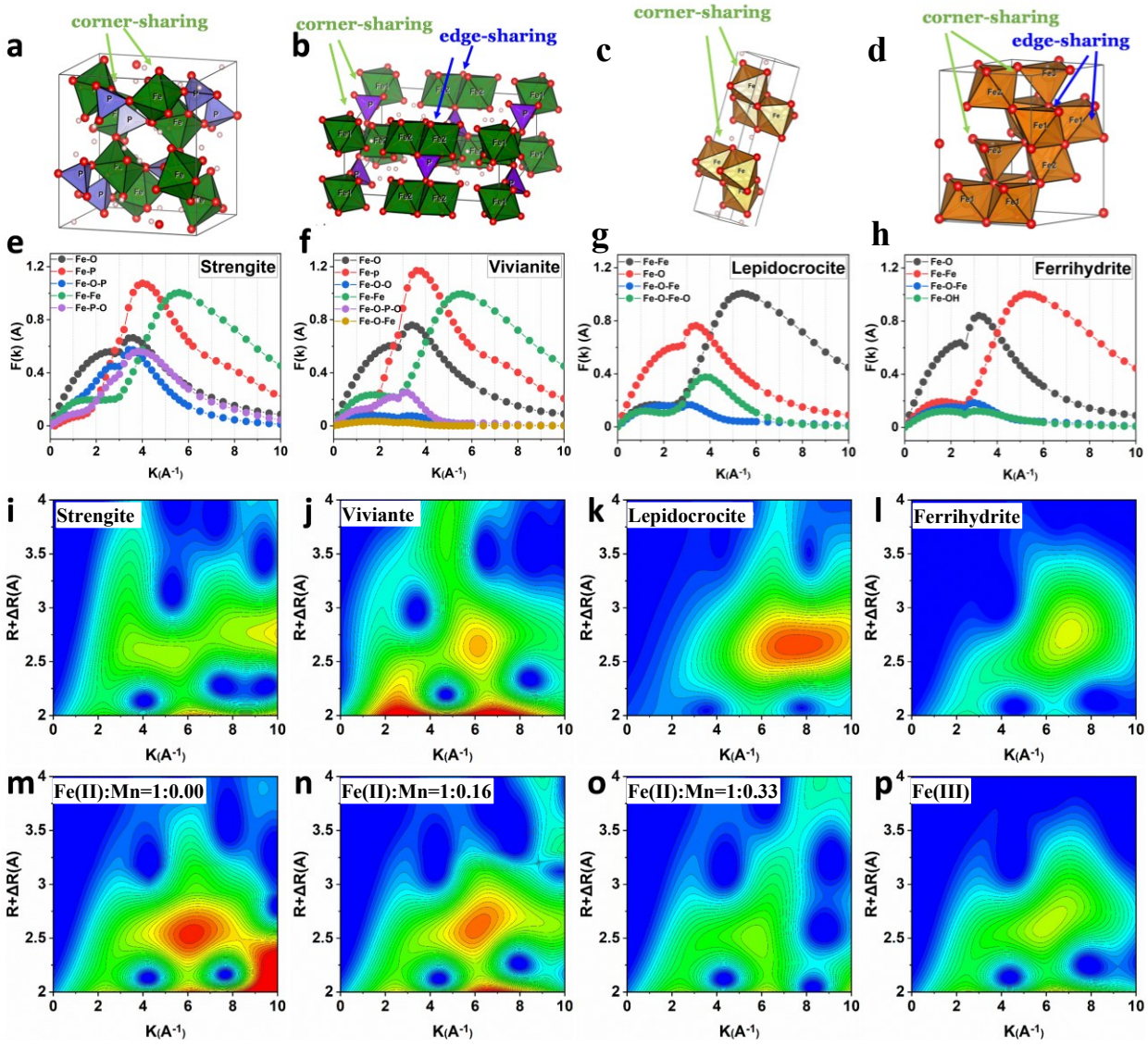

709

710 **Fig. 4: Model structure and wavelet transform results of minerals and flocs.** Crystal models of

711 selected standard minerals (a~d). Their backscattering amplitude factors associated with the elements

712 present in the system calculated by FEFF6 (e~h). High-resolution wavelet transform plots of standards

713 minerals (i~l) and flocs formed by different coagulants (m~p) in the second and third shells, η = 8 and

714 σ = 1. Data are plotted as k(Å–1) on the x-axis and R (Å) on the y-axis in the range 2.0–4.0 (Å).

715

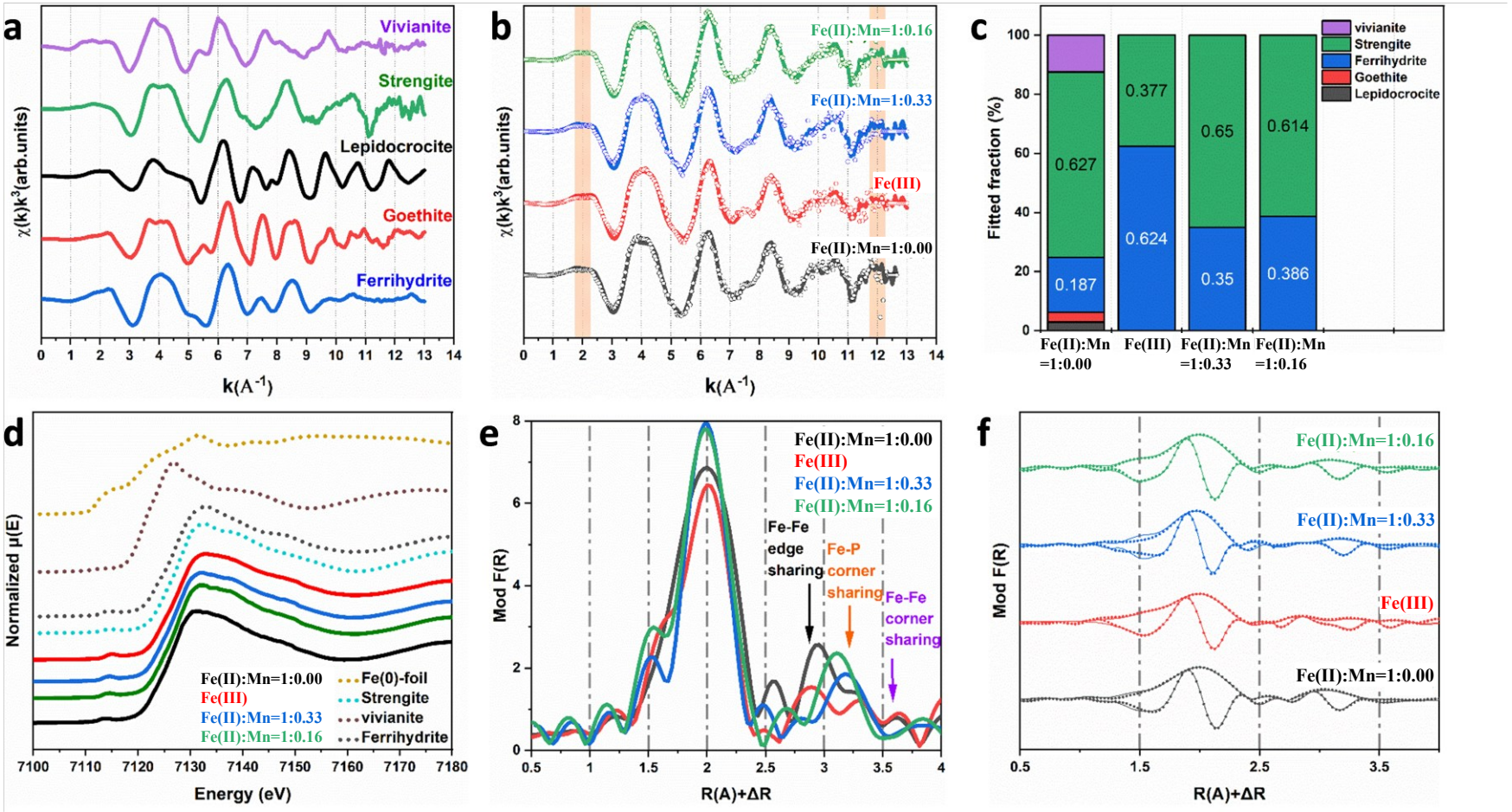

Fig. 5: Impact of the slip length on the platelet dynamics. Fe k3-weighted EXAFS spectra of reference minerals (a) and floc samples (b). Dotted lines show real data and solid lines show linear combination fits over a k-range of 2–12 $Å^{-1}$ using reference as fit components. Linear combination fitting (LCF) results of EXAFS (c). Fe K-edge XANES of Fe(o)-foil reference, mineral references, and flocs (d). Fourier-transformed magnitude spectra (e) and real part (f) in R space.